J. Fluid Mech. (2001), *vol.* 435, *pp.* 327–350. Printed in the United Kingdom

On the displacement of three-dimensional fluid droplets adhering to a plane wall in viscous pressure-driven flows

By P. DIMITRAKOPOULOS† AND J. J. L. HIGDON

Department of Chemical Engineering, University of Illinois, Urbana, IL 61801, USA

(Received 22 February 2000 and in revised form 1 December 2000)

The yield conditions for the displacement of three-dimensional fluid droplets adhering to a plane solid boundary in pressure-driven flows are studied through a series of numerical computations. The study considers low-Reynolds-number flows between two parallel plates and includes interfacial forces with constant surface tension. A comprehensive study is conducted, covering a wide range of viscosity ratio λ, capillary number Ca, advancing and receding contact angles, θ_A and θ_R, and dimensionless plate separation H/h (where H is the plate spacing and h is the unperturbed droplet height). This study seeks the optimal shape of the contact line which yields the maximum flow rate (or Ca) for which a droplet can adhere to the surface. The critical shear rates are presented as functions $Ca(\lambda, H/h, \theta_A, \Delta\theta)$ where $\Delta\theta = \theta_A - \theta_R$ is the contact angle hysteresis. The numerical solutions are based on an efficient, three-dimensional Newton method for the determination of equilibrium free surfaces and an optimization algorithm which is combined with the Newton iteration to solve the nonlinear optimization problem. The critical shear rate is found to be sensitive to viscosity ratio with qualitatively different results for viscous and inviscid droplets. As the viscosity of a droplet increases, the critical flow rate decreases, facilitating the displacement. This is consistent with our previous results for shear flows (Dimitrakopoulos & Higdon 1997, 1998), which represent the limit of infinite plate spacing. As the plate spacing is reduced, the critical flow rate increases until a maximum value is reached. Further reduction in the plate spacing decreases the critical flow rate. The effects of both viscosity ratio and plate separation are much more pronounced for high contact angles. Inviscid droplets (or bubbles) show behaviour dramatically different from that of viscous droplets. For these droplets, a significantly higher flow rate is required for drop displacement, but this critical flow rate decreases monotonically as the distance between the plates decreases. In the Appendix, we clarify the necessary conditions for low-Reynolds-number flows past low viscosity droplets or bubbles.

1. Introduction

In this paper, we study the yield conditions for the displacement of three-dimensional fluid droplets adhering to a single wall in pressure-driven flows between parallel plates at low Reynolds number. This problem serves as a prototype for similar flows encountered in manufacturing processes in the coating industry, as well as for

† Present address: Division of Chemistry and Chemical Engineering, California Institute of Technology, Pasadena, CA 91125, USA.

drop displacement problems relevant to enhanced oil recovery. Previous work in this area has concentrated on the problem of drop displacement by viscous shear flows. The fundamental issues associated with shear-induced displacement have been discussed in Dussan V. (1987) and in our own earlier work (Dimitrakopoulos & Higdon 1997, 1998, hereafter referred to as DH1 and DH2 respectively). In these papers, we conducted an extensive numerical investigation of the drop displacement problem, discussed scaling laws based on the underlying physics and showed how the scaling analysis explained the qualitative trends observed in the numerical simulations. We found excellent agreement with Dussan V.'s asymptotic theory, but showed that the asymptotic results were of limited utility for quantitative predictions at finite values of the advancing contact angle θ_A and contact angle hysteresis $\theta_A - \theta_R$. A detailed discussion of these points and a review of other literature relevant to this problem may be found in these earlier papers.

In more recent work, a number of researchers have considered variations on the drop displacement problem. Yon & Pozrikidis (1999) studied the shear-induced deformation of three-dimensional droplets adhering to solid substrates with fixed contact lines. These authors extended an earlier effort by Li & Pozrikidis (1996) to include the influence of the viscosity ratio λ and the effect of insoluble surfactants on the droplet deformation. Schleizer & Bonnecaze (1999) studied the problem of droplet displacement in both shear- and pressure-driven flows. They limited their study to two-dimensional droplets analogous to DH1 and considered displacement criteria for fixed contact points. Schleizer & Bonnecaze also studied the case of droplets sliding smoothly over the solid surface and included the effects of surfactants on the droplet deformation. Dimitrakopoulos & Higdon (1999) complemented earlier work on shear-induced displacement by analysing drop displacement induced by gravitational forces in a quiescent fluid.

In the present paper, we turn our attention to the displacement of three-dimensional droplets from solid boundaries in pressure-driven flows. To date, there has been no study which addresses the full three-dimensional formulation of this important problem. To address this challenge, we employ a three-dimensional Newton method to compute the equilibrium shape of the fluid interfaces, combined with an optimization algorithm to determine the optimal contour for the contact line on the solid substrate. This optimal contact line is defined as that contour which requires the greatest hydrodynamic force to displace a droplet with given size and material properties. The numerical methods have been well documented in our recent paper on shear-induced displacement (DH2) and will not be discussed in detail in the present effort.

2. Mathematical formulation and numerical methods

We consider a three-dimensional droplet immersed in a low-Reynolds-number flow between parallel plates positioned at $z = 0$ and $z = H$. The droplet is attached to the lower plate as illustrated in figure 1. The droplet size is specified by its volume V_0 or equivalently by the radius a of a spherical droplet of volume $V_0 = (4\pi/3)a^3$. The droplet (fluid 1) has density ρ_1 and viscosity $\lambda\mu$, while the surrounding fluid (denoted as fluid 2) has density ρ_2 and viscosity μ. The surface tension γ is assumed constant and we neglect gravitational forces, considering fluids with the same density or very small droplets. The undisturbed flow far from the droplet is a plane Poiseuille flow $\boldsymbol{u}^\infty = G\,(z - z^2/H, 0, 0)$ where the constant G is the velocity gradient $(\mathrm{d}u_x/\mathrm{d}z)_{z=0}$ at the lower wall. The contact line forms a closed curve C in the (x, y)-plane which intersects

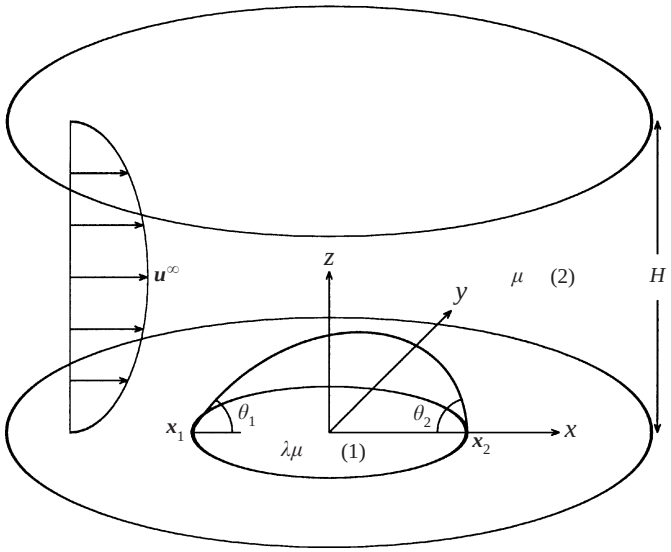

FIGURE 1. Pressure-driven flow between two parallel plates past a fluid droplet attached to the lower plate.

the x-axis at two points, with the upstream point and contact angle designated $\boldsymbol{x}_1$ and θ_1, and the corresponding downstream ones $\boldsymbol{x}_2$ and θ_2.

The capillary number Ca, representing the ratio of the viscous forces to interfacial forces, is defined by

$$Ca = \frac{\mu Ga}{\gamma}.$$

The governing equations in the infinite fluid are the Stokes equations together with continuity

$$\nabla \cdot \boldsymbol{\sigma} = -\nabla p + \mu \nabla^2 \boldsymbol{u} = 0, \tag{1}$$

$$\nabla \cdot \boldsymbol{u} = 0, \tag{2}$$

with similar expressions for the droplet, with the viscosity replaced by $\lambda\mu$. In the Appendix of this paper, we present the necessary conditions for low-Reynolds-number exterior and interior flows.

The boundary conditions on the solid walls and at infinity give

$$\boldsymbol{u} = 0 \quad \text{on} \quad z = 0 \text{ and } z = H, \tag{3}$$

$$\boldsymbol{u} \to \boldsymbol{u}^\infty \quad \text{as} \quad r \to \infty. \tag{4}$$

At the interface, the boundary conditions on the velocity $\boldsymbol{u}$ and surface stress $\boldsymbol{f}$ are

$$\boldsymbol{u}_1 = \boldsymbol{u}_2, \tag{5}$$

$$\boldsymbol{f}_2 - \boldsymbol{f}_1 = \gamma(\nabla \cdot \boldsymbol{n})\boldsymbol{n}. \tag{6}$$

Here the subscripts designate quantities evaluated in fluids 1 and 2 respectively. The surface stress is defined as $\boldsymbol{f} = \boldsymbol{\sigma} \cdot \boldsymbol{n}$, and $\boldsymbol{n}$ is the unit normal which we choose to point into fluid 2.

For *equilibrium shapes*, the velocity field must satisfy an additional constraint – the

kinematic condition at the interface

$$\boldsymbol{u}_1 \cdot \boldsymbol{n} = \boldsymbol{u}_2 \cdot \boldsymbol{n} = 0. \tag{7}$$

Note that we define an *equilibrium* shape to be a stationary interface for which all kinematic and dynamic boundary conditions are satisfied under conditions of steady flow. This should not be confused with the concept of equilibrium surfaces under quiescent conditions.

For droplets in contact with a solid boundary, additional conditions are required to prescribe the interface shape in the vicinity of the contact line. For real surfaces (i.e. rough and chemically inhomogeneous), it has been found that the static contact angle exhibits a hysteresis effect where the contact line remains stationary for any angle in the range

$$\theta_R \leqslant \theta \leqslant \theta_A. \tag{8}$$

The limits θ_A and θ_R are called the advancing and receding angles respectively. As in DH2, we assume that the advancing and receding angles θ_A and θ_R are physical constants and require that (8) hold for all angles along the contact line C. More details and references concerning the phenomenon of contact angle hysteresis as well as the boundary conditions along the contact line can be found in our earlier papers (DH1, DH2).

The relevant parameters in this problem include those of the problem of droplet displacement in viscous shear flows (DH2); namely, the capillary number Ca, the viscosity ratio λ, the advancing contact angle θ_A and the receding contact angle θ_R or equivalently the hysteresis $\theta_A - \theta_R$. An additional parameter in the current problem is the plate separation non-dimensionalized as H/h, where h is the height of the fluid droplet in the quiescent fluid. In the absence of gravity, the undisturbed droplet takes the form of a spherical cap with a constant contact angle along a circular contact line. The constant angle θ may take any value in the range $\theta_R \leqslant \theta \leqslant \theta_A$; however we assume that the procedure for establishing the initial state yields a value $\theta = \theta_A$. (See the extensive discussion in DH2 on this issue.) The droplet height h is given by $h = R_0\ (1 - \cos\theta_A)/\sin\theta_A$, where R_0 is the radius of the undisturbed contact line and is related to the characteristic radius a via the relation $(4\pi/3)a^3 = V = (\pi/3)R_0^3(2 - 3\cos\theta_A + \cos^3\theta_A)/\sin^3\theta_A$.

The problem formulation given by equations (1)–(8) is analogous to that arising for shear-induced displacement presented in DH2. The computational procedures are similar and only a brief description will be given here.

The determination of the yield conditions for drop displacement may be formulated as an optimization problem in the following form: for a given contact angle θ_A and hysteresis $\theta_A - \theta_R$, find the configuration corresponding to the highest capillary number Ca for which an equilibrium solution exists. An alternative, but equivalent, problem may be stated: for a given contact angle θ_A and capillary number Ca, find the configuration corresponding to the minimum $\theta_A - \theta_R$ for which an equilibrium solution exists. This latter form proves more convenient for numerical computations and has been adopted in our work; however, the results may be viewed in either context with equal validity.

The solution to the optimization problem gives the critical condition for drop displacement in terms of the maximum capillary number Ca or minimum contact angle hysteresis $\theta_A - \theta_R$. Unfortunately, the optimal configuration and associated yield condition may not be realized in an experiment. Depending upon the initial configuration of the droplet, its initial deformation may lead to elongation in the flow

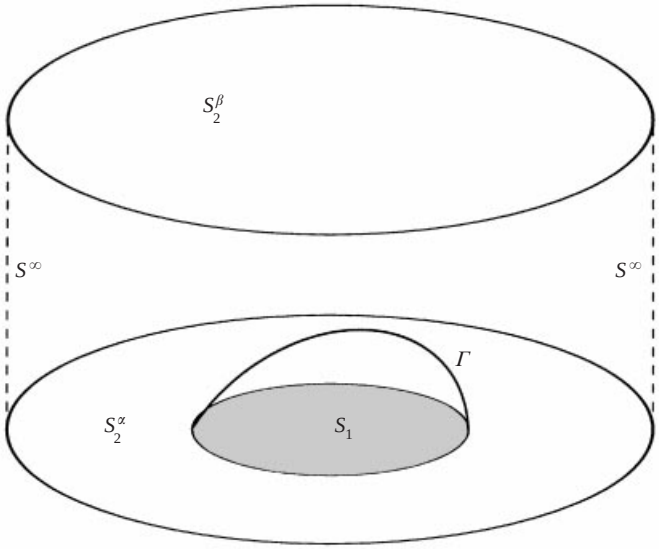

FIGURE 2. Domain geometry for boundary integral solution for pressure-driven flow between two parallel plates past a droplet attached to the lower plate.

direction, and it may be unable to access the optimal configuration. To determine the critical yield conditions in such experiments, we reformulate the optimization problem above with the additional constraint that the magnitude of the lateral positions y cannot exceed the maximum value $|y_0^{max}|$ in the initial configuration of the droplet. This optimization will be called the *y-constrained* optimization problem while the previous problem will be called the *unconstrained* optimization problem. More details concerning the two optimization problems can be found in our earlier paper (DH2, §§ 2.3 and 3.1).

The boundary integral formulation employed here is similar to that described in DH2, § 2.1. The surfaces specifying the boundaries of the fluid domain are identified in figure 2. With a formulation based on the disturbance velocity $\boldsymbol{u}_2^D = \boldsymbol{u}_2 - \boldsymbol{u}^\infty$ the integral on S^∞ vanishes as its radius approaches infinity. While the radius of surfaces S_2^α and S_2^β extends to infinity in this case, a finite radius is employed in practice. Extensive tests were conducted to evaluate the associated error with the radius of S_2^α and S_2^β ranging from 3 to 40 times the radius r of the contact region. It is found that a radius equal to $5r$ is sufficient to produce a change in the critical hysteresis angle of less than 1%, while a radius of $10r$ yields a relative error of less than 10^{-3}. Given these results, a radius of $10r$ was chosen for all computations in this paper.

In the present paper, the majority of computations were performed with a discretization employing 33 elements. The drop surface Γ and the solid surfaces S_1 and S_2^α are discretized into 11, 5 and 8 elements respectively, as discussed in DH2 (see their figure 3*a*, *b*). The upper wall S_2^β is divided into 9 elements with a discretization similar to that of the lower wall. For values of $H/h < 1.1$, an additional row of four elements is inserted on the top wall above the droplet.

For the majority of the results presented in this paper, a spectral expansion with $N_B = 7$ points was used on each element. For certain cases with $\theta_A = 50°$, additional points were used up to $N_B = 9$. For $\theta_A = 30°$, the hysteresis $\theta_A - \theta_R$ and the jump in the distribution of the contact angles (see figure 3*c* below) are small; however,

many points are required throughout the drop surface. In this case, the drop surface was divided into five elements with $N_B = 10$. Convergence for the spectral element computations and for the optimization procedure was verified by increasing the number of spectral points N_B and determining the change in the computed hysteresis $\theta_A - \theta_R$. In all cases, the results show a rapid decrease in the discretization error with increasing number of basis points, similar to that presented in DH2, table 1 for the problem of drop displacement in viscous shear flows.

The problem studied in this paper admits one level of symmetry about the plane $y = 0$. Exploiting this symmetry reduces the memory requirements by a factor of 2^2, the computational time for the system matrices by a factor of 2 and the solution time for the linear systems by factor of 2^3. All the computations were performed on the multiprocessor computers SGI Cray Origin 2000 and HP-Convex Exemplar SPP 2000, provided by the National Center for Supercomputing Applications. Multiprocessor runs exploit the parallel nature of calculating the system matrices resulting in a nearly linear decrease in c.p.u. time.

3. Results

In the following subsections, we determine the optimal shape of the contact line which gives the maximum flow rate (or Ca) for which a droplet can adhere to a boundary wall in pressure-driven flows. We conduct a detailed study of the relevant parameters, presenting results for the critical Ca as a function of hysteresis $\theta_A - \theta_R$ for several fixed values of the advancing contact angle θ_A, the viscosity ratio λ and the plate separation H/h. While we consider the effect of all parameters on the problem, we are most interested in the influence of the plate separation H/h on the critical flow rate. As the plate separation approaches infinity, the pressure-driven flow near the walls approaches a simple shear flow, and the computations reproduce the shear flow results of DH2. In § 3.1 we study the yield conditions for drop displacement and the influence of the plate separation H/h for viscous droplets. In § 3.2, we turn our attention to inviscid droplets ($\lambda = 0$) while in § 3.3 we consider the effect of varying the viscosity ratio while maintaining a fixed plate spacing H/h. In § 3.4, we make a brief comparison with experiments.

3.1. *Displacement of viscous droplets*

We begin our investigation of drop displacement in pressure-driven flows by studying viscous droplets with $\lambda = 1$ and $\theta_A = 90^\circ$. Figure 3(a, b) shows the contact line contours and the drop profiles (drop surface intersection with the plane $y = 0$) for the unconstrained optimization problem for plate spacing $H/h = 2$ and for several values of the capillary number Ca. In figure 3(b), the upper plate lies at $z = 2$, above the top of the figure. (As implemented in this paper, the height of the quiescent droplet with $\theta_A = 90^\circ$ is $h = 1$.) Each successive curve corresponds to a higher Ca and a larger contact angle hysteresis is required to hold the drop in place.

As the hydrodynamic forces on the droplet increase, the counterbalancing interfacial force increases by reducing the contact angle on the front of the droplet. This brings the interfacial force vector more nearly parallel to the plane and in opposition to the hydrodynamic force. With a smaller angle, the droplet spreads over a larger area to accommodate the fluid volume. Note that the width of the contact line in the y-direction increases more than the extension in the x-direction. As explained in DH2, the net interfacial force is proportional to $\theta_A - \theta_R$ and the width of the contact

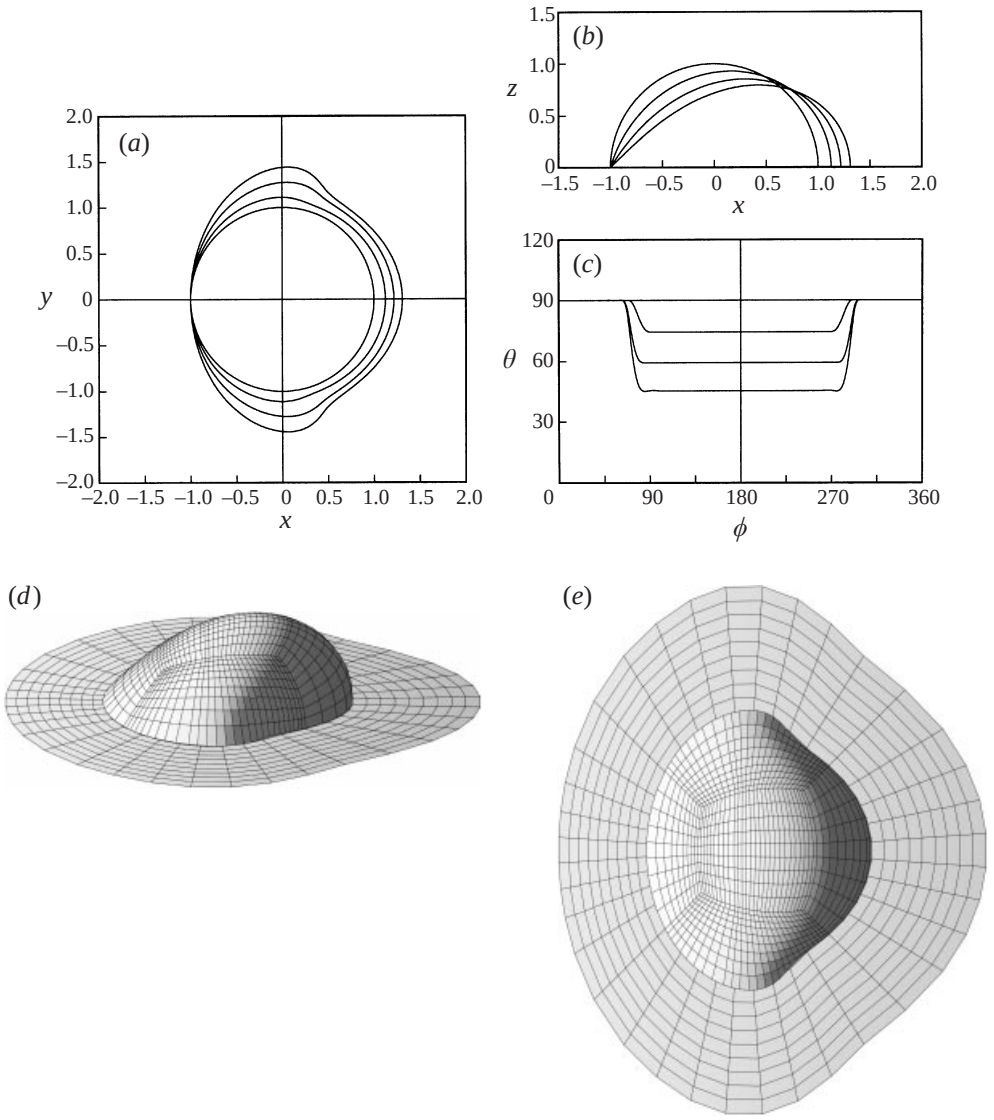

FIGURE 3. Equilibrium shapes for droplets in pressure-driven flows with viscosity ratio $\lambda = 1$ and advancing contact angle $\theta_A = 90°$, for $H/h = 2$ and for the unconstrained optimization problem. For (*a–c*) the capillary number is $Ca = 0, 0.04, 0.08, 0.115$. (*a*) The optimal shape of the contact line. (*b*) The cross-section of the drop surface with the plane $y = 0$. (*c*) The variation of the contact angle θ as a function of the azimuthal angle ϕ. (*d, e*) The drop surface for capillary number $Ca = 0.115$.

line. The increased width and the reduced contact angle act together to increase the interfacial force, yielding the wide asymmetrical profile illustrated in figure 3(*a*).

While we have focused on the shape of the contact line, the variation of the contact angle around the contour also has an important effect on the force balance. Figure 3(*c*) shows the contact angle θ along the contact line as a function of the azimuthal angle ϕ measured with respect to the positive x-direction. In this figure, the downstream portion of the contact line maintains a constant contact angle equal to the maximum allowable value θ_A, while the upstream portion maintains a constant value equal to the minimum angle θ_R. Between these two sections there is a rapid jump in the contact

angle over the short segments $\phi \approx 65°$–$90°$ and $\phi \approx 270°$–$295°$. For fixed values of λ, θ_A and Ca, the jump occurs at approximately the same ϕ location independent of the plate spacing H/h. This is easily verified by comparing figure 3(c) with figure 4(c) in DH2. The sharp jump in contact angle is a consequence of the droplet's attempts to maximize the interfacial force. The drop holds the minimum contact angle over the entire front of the contact line, then makes the fastest possible transition to the maximum angle on the rear-facing contour. A three-dimensional illustration of the drop surface is shown in figure 3(d, e).

While the contours seen in the figures above represent the most stable contact lines a droplet may achieve, they are not necessarily the contours which will be seen in experiments. If a droplet is placed in a quiescent fluid with initial contact angle θ_A and the fluid velocity is slowly increased, the rear of the droplet may yield first, leading to extension in the flow direction. The optimal contact line contours may not be accessible to the droplet in that particular experiment. As explained in DH2, § 3.1, the actual yield stress is determined not only by the maximum possible yield stress, but also by the initial configuration of the droplet, the conditions of the experiment and the evolution of the contact line. To test the sensitivity of the yield stress under these conditions, we consider the *y-constrained* optimization problem as described in § 2. For this problem, we assume that the experimental conditions constrain the contact line to displacements in the flow direction, and we require that the y-positions do not exceed their maximum initial extension.

Figure 4(a, b) shows the contact line contours and the drop profiles for the y-constrained optimization at several values of Ca for the same droplet and plate spacing as above. As with the unconstrained optimization, for each successive curve, a larger contact angle hysteresis is required to offset the increased flow rate. Figure 4(a) shows that the downstream portion of the contact line is displaced much further for the y constrained droplets compared to the unconstrained droplets at the same capillary number.

Figure 4(c) shows the contact angle θ along the y-constrained contact line as a function of the azimuthal angle ϕ. As before, the downstream portion of the contact line maintains a constant angle θ_A, the upstream portion holds to a constant angle θ_R, and there is a rapid transition over the sections $\phi \approx 60°$–$120°$ and $\phi \approx 240°$–$300°$. The broader width of the transition region for the y-constrained droplets is attributable to the elongated shape of the contact line; that is, for drops with long sides parallel to the flow direction, the net interfacial force is insensitive to the position and width of the jump, because the interfacial force acts in a lateral direction on these sections. It is of interest to note that the ovoid shape of the y-constrained contact line cannot be approximated with an ellipse, because the contact angles on an ellipse change more smoothly along the contact line. In addition, the minimum angle θ_R for an ellipse is located not on the upstream portion of the contact line but somewhere between the upstream and the downstream portions (see Li & Pozrikidis 1996, figure 12f).

Figure 4(d, e) shows three-dimensional views of a y-constrained drop for $Ca = 0.10$. Comparison with the three-dimensional views of the optimal configuration in figure 3 shows the obvious differences for the two optimization problems. In comparing the yield conditions for y-constrained and unconstrained droplets, we find that the y-constrained contact line requires a slightly larger hysteresis $\theta_A - \theta_R$ to hold its position, i.e. it is slightly less stable than the optimal configuration.

Having explored the basic principles associated with the deformation and displacement of the droplet, we turn our attention to the prediction of the yield conditions as a function of the drop parameters. Figure 5 shows the critical Ca as a function of

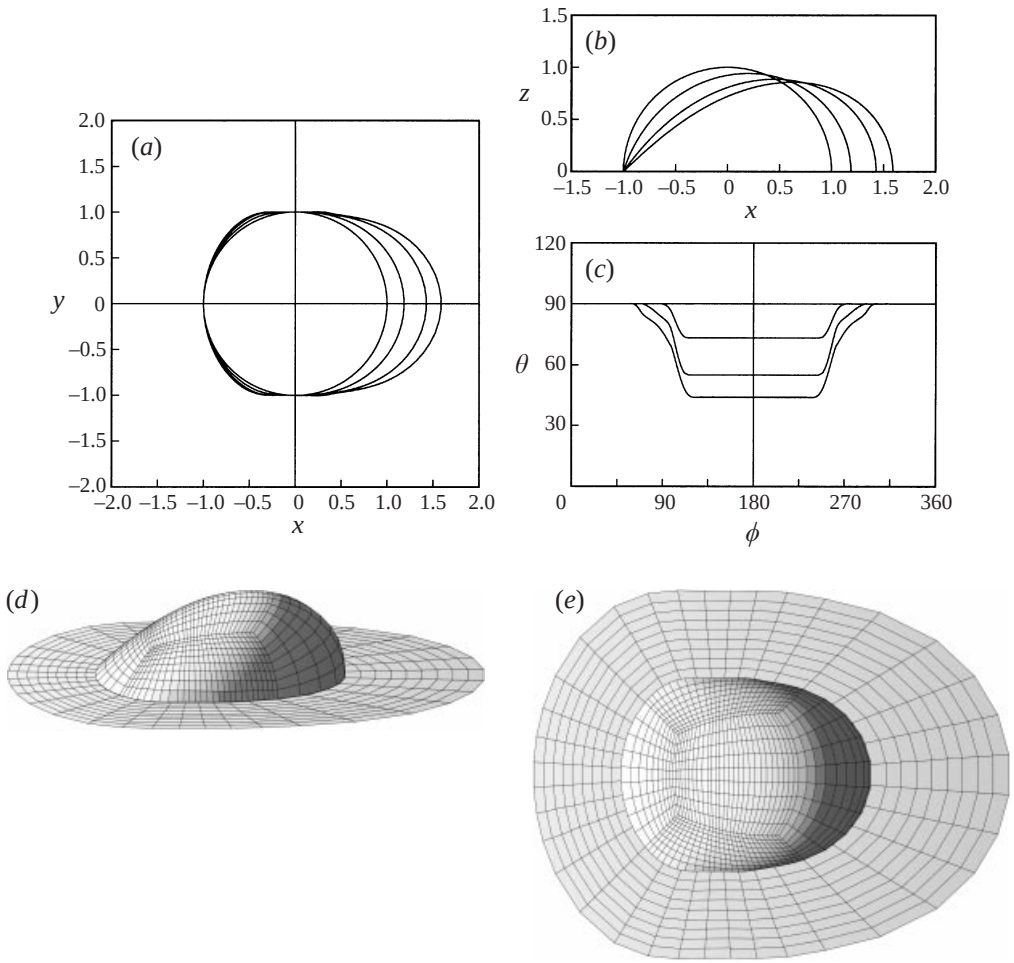

FIGURE 4. Equilibrium shapes for droplets in pressure-driven flows with viscosity ratio $\lambda = 1$ and advancing contact angle $\theta_A = 90°$, for $H/h = 2$ and for the y-constrained optimization problem. For (a–c) the capillary number is $Ca = 0, 0.04, 0.08, 0.10$. (a) The optimal shape of the contact line. (b) The cross-section of the drop surface with the plane $y = 0$. (c) The variation of the contact angle θ as a function of the azimuthal angle ϕ. (d, e) The drop surface for capillary number $Ca = 0.10$.

the contact angle hysteresis for the unconstrained and y-constrained optimal contact lines. In this figure, we plot one additional curve, corresponding to the case of a circular contact line. This last curve is determined as the solution of an optimization problem for contact lines of circular shape but arbitrary radius (DH2, § 3.3). The insets show the actual shape of the contact line contours and the droplet profiles for the three different configurations at a typical value of Ca. For each point on a given curve, we specify the capillary number and a fixed value of θ_A, and find the optimal solution which minimizes the hysteresis $\theta_A - \theta_R$. The specified Ca then represents the yield condition for that value of θ_A and $\theta_A - \theta_R$. The terminal points at the end of each curve represent the largest $\theta_A - \theta_R$ for which accurate numerical calculations could be executed. The criteria for an accurate numerical solution include convergence of the linear programming iteration and of the Newton iteration, consistency with increasing order of N_B and an error tolerance for the maximum $\boldsymbol{u} \cdot \boldsymbol{n} \neq 0$ on

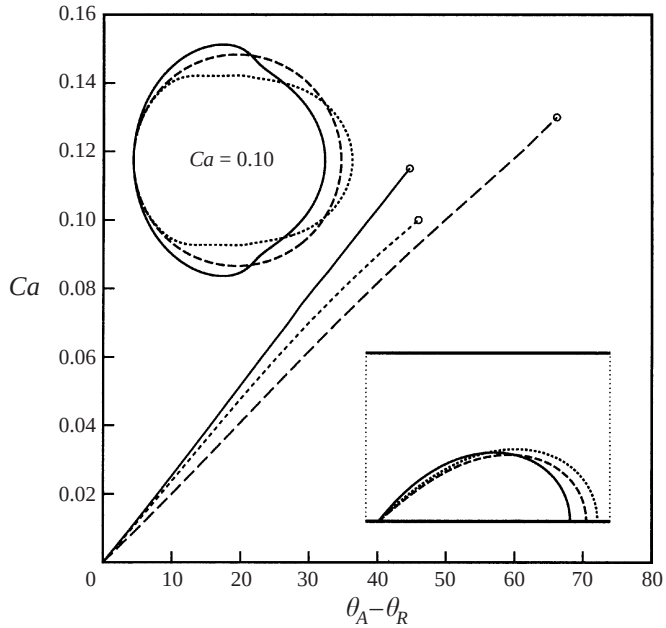

FIGURE 5. Critical capillary number Ca versus hysteresis $\theta_A - \theta_R$ for $\lambda = 1$, $\theta_A = 90°$, $H/h = 2$ and for different optimal contact lines. Also shown are the shapes of the contact line as well as the drop profiles for $Ca = 0.10$. Contact lines: ——, unconstrained; - - - -, y-constrained; – – – –, circular.

the interface. For all cases, the algorithm stops when the linear programming fails to converge. On physical grounds, we expect that the true terminal point corresponds to a value $\theta_A - \theta_R \to \theta_A$, for which $\theta_R \to 0$ and the interface becomes tangent to the boundary wall at the upstream portion of the contact line. We emphasize that figure 5 gives accurate yield conditions for all parameter values shown. The only limitation is that we are unable to provide precise predictions for extreme values of the hysteresis $\theta_A - \theta_R$. The results shown in figure 5 demonstrate that the critical capillary number Ca for the unconstrained optimization problem is consistently higher than for the other two problems. As the contact angle θ_A decreases, the difference in Ca for the unconstrained and the y-constrained problem becomes smaller and smaller. For all angles θ_A studied, we found that the circular contact line admits a significantly smaller capillary number. For a droplet free to move over a solid surface, these results show that the assumption of a circular contact line predicts a measurably smaller yield stress than would be achieved in practice.

We now turn our attention to the effect of the advancing contact angle θ_A on the critical capillary number. For brevity, we show results for the unconstrained droplets only; additional results may be found in Dimitrakopoulos (1998). Figure 6 shows the yield conditions for droplets with different values of θ_A as a function of hysteresis. This figure shows that, at the specified plate spacing $H/h = 2$, the influence of the contact angle θ_A on the yield condition is similar to its effect in simple shear flows (DH2, § 3.1). In particular, for a given hysteresis $\theta_A - \theta_R$, increasing the contact angle θ_A from small values, increases the critical flow rate, up to $\theta_A \approx 90°$. Above this value, increasing the contact angle θ_A decreases the critical flow rate.

The explanation for the contact line dependence becomes clear when one considers the three forces which act upon the droplet: viscous shear stress, pressure forces and interfacial force. For viscous droplets with small advancing contact angle ($\theta_A \ll 1$), the

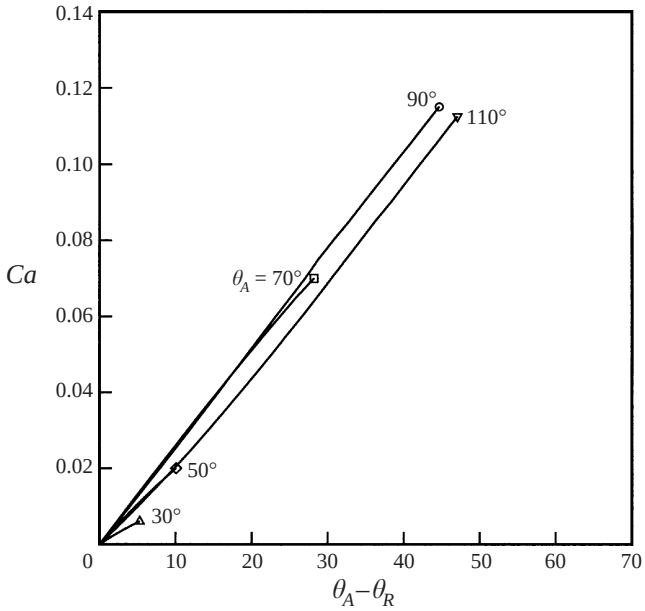

FIGURE 6. Critical capillary number Ca versus hysteresis $\theta_A - \theta_R$ for viscosity ratio $\lambda = 1$, plate separation $H/h = 2$, for the unconstrained optimization problem and for different advancing angles θ_A.

shear stress scales as $\tau_\infty \equiv \mu G$ independent of the internal viscosity. The corresponding force is proportional to the surface area of the droplet and scales as $\tau_\infty r^2$, where r is the radius of the contact region. In terms of the characteristic radius a based on drop volume, this gives $\tau_\infty a^2 \theta_A^{-2/3}$.

The pressure forces on the droplet may be divided into two distinct components. The first term arises from the undisturbed pressure gradient acting on the droplet. The pressure gradient in the flow scales as $\tau_\infty H^{-1}$, and the pressure change Δp over the droplet scales as $\tau_\infty \ell H^{-1}$, where ℓ is the length of the droplet in the flow direction. The pressure force scales as Δp times the frontal area of the drop yielding $\tau_\infty \ell H^{-1}$ (wh), where w is the width of the contact line and h the drop height under quiescent conditions. In terms of the characteristic drop radius a, the pressure force scales as $\tau_\infty H^{-1} a^3$. For fixed values of the dimensionless spacing H/h, the plate spacing relative to fixed drop size H/a and the associated pressure gradient will change with the value of the advancing angle θ_A. Thus we may write the pressure force in the alternative form $\tau_\infty a^2 \theta_A^{-2/3} (H/h)^{-1}$.

The second component of the pressure force arises from the disturbance of the base flow owing to the presence of the droplet. The pressure change Δp for this term scales as $\tau_\infty \theta_A$ and the associated pressure force scales as $\tau_\infty \theta_A$ (wh) or $\tau_\infty a^2 \theta_A^{4/3}$. For a viscous droplet and for all plate spacings H/h, the second component of the pressure force is much smaller than the viscous shear stress. On the other hand, the pressure force associated with the undisturbed pressure gradient is small compared to the shear stress for large plate spacing ($H/h \gg 1$). As the plate spacing decreases, this pressure force increases and for $H/h \sim O(1)$ it scales as the viscous shear stress. Thus for all viscous droplets, the net hydrodynamic force scales as $\tau_\infty a^2 \theta_A^{-2/3}$, which is consistent with the scaling for shear flows found in DH2.

Balancing the hydrodynamic force is the component of interfacial force in the plane of the wall parallel to the flow direction. This force is proportional to the width of the contact region and, for small hysteresis $\theta_A - \theta_R$, it scales as $(\cos\theta_R - \cos\theta_A)\,\gamma w$. For small contact angles and small hysteresis, this force takes the asymptotic form $(\theta_A - \theta_R)\theta_A \gamma r \sim (\theta_A - \theta_R)\gamma a \theta_A^{2/3}$. As θ_A increases, the hydrodynamic force decreases as $\theta_A^{-2/3}$, while the interfacial force increases as $\theta_A^{2/3}$. Thus a higher shear rate is required to dislodge the droplet when θ_A increases from small values, in agreement with our results in figure 6. A balance of these two forces gives the scaling for the critical capillary number

$$Ca_{asym\_viscous} \sim \theta_A^{4/3}\,(\theta_A - \theta_R). \tag{9}$$

When the contact angle θ_A approaches 90°, the interfacial force $(\cos\theta_R - \cos\theta_A)\,\gamma w$ reaches its maximum value. Higher contact angles reduce the net interfacial force leading to the reduction in critical flow rate seen in figure 6 above. A comparison between the scaling predictions and the numerical results shows good agreement in the relevant asymptotic limits (i.e. for $\theta_A - \theta_R \ll \theta_A \ll 1$). This has been shown previously in our study on shear flows (see DH2, figure 15) and similar agreement holds for the pressure-driven flows considered here. For larger contact angles, the quantitative agreement is rather poor; however the scaling analysis predicts the correct qualitative behaviour in all cases.

Having considered the displacement of droplets for $H/h = 2$, we now turn our attention to the effects of plate spacing H/h. As the plate separation H/h approaches infinity, the pressure-driven flow near the walls approaches a simple shear flow, and the results are consistent with the shear flow results in DH2. As an example, for a droplet with $\lambda = 1$, $\theta_A = 90°$ at a given Ca, the critical hysteresis for pressure-driven flow differs from the shear flow result by a relative change of less than 7×10^{-3} for $H/h = 50$, and less than 3×10^{-3} for $H/h = 100$.

Figure 7(*a*) shows the critical Ca as a function of hysteresis $\theta_A - \theta_R$ for several values of H/h. This figure exhibits an interesting trend in the dependence of the critical condition for a viscous droplet on plate spacing. For a given hysteresis $\theta_A - \theta_R$, the critical Ca increases as the plate spacing is reduced from ∞ until it reaches a maximum around $H/h = 2$. This implies that a plate spacing of $H/h = 2$ has the most stable droplets. Below this plate spacing, the critical Ca decreases, reaching a limiting value as $H/h \to 1$. The dependence of yield condition on plate spacing is illustrated more clearly in figure 7(*b*), which shows the critical hysteresis as a function of plate separation for a representative capillary number. The existence of a minimum in this curve (and the corresponding maximum in Ca in figure 7*a*) may be understood by considering the individual contributions to the hydrodynamic force. The pressure force associated with the applied pressure gradient increases monotonically as H/h decreases owing to the increasing pressure gradient ($\tau_\infty H^{-1}$). The force due to viscous shear stress decreases as the plate spacing is reduced. At infinite spacing the stress on the droplet is very close to τ_∞, but as the top plate is brought closer, it shields the drop surface and the shear stress is reduced. For viscous drops, the combination of these trends yields a minimum in hydrodynamic force near $H/h = 2$. For inviscid drops considered below, we shall see a monotonic dependence on plate spacing.

The influence of plate spacing on three-dimensional droplets is in contrast to the results for two-dimensional droplets where a monotonic decrease in the yield stress with H/h is found (see Schleizer & Bonnecaze 1999, their figure 6). For two-dimensional droplets, the entire volume of fluid must flow through the narrow gap above the droplet. Owing to this feature, both the pressure force and the shear stress

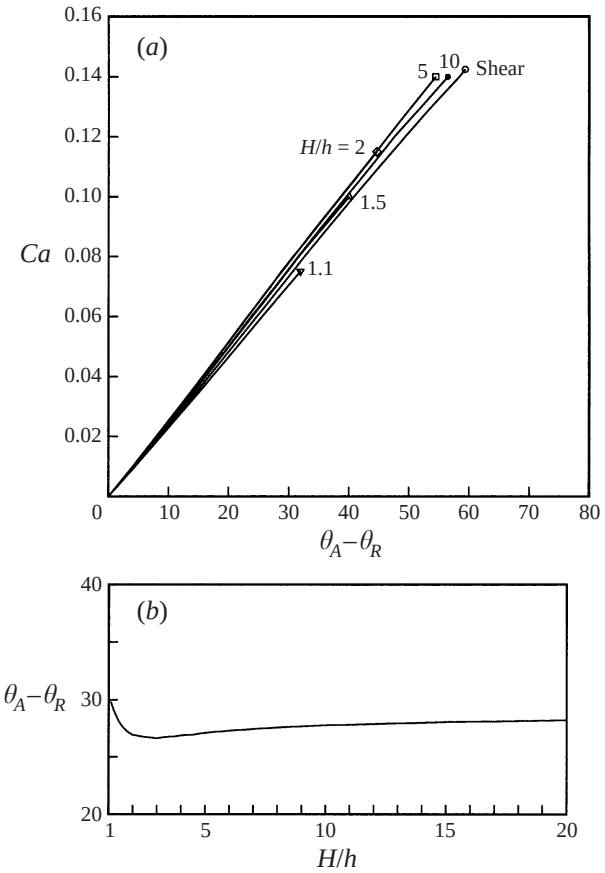

FIGURE 7. Influence of the plate separation H/h. (*a*) Critical capillary number Ca versus hysteresis $\theta_A - \theta_R$ for a droplet with $\lambda = 1$ and $\theta_A = 90°$, for the unconstrained optimization and for different plate separations H/h. (*b*) Contact angle hysteresis $\theta_A - \theta_R$ versus plate separation H/h for a droplet with $\lambda = 1$ and $\theta_A = 90°$, for $Ca = 0.07$ and for the unconstrained optimization.

increase as the plate spacing is reduced. For three-dimensional droplets, the fluid simply flows around the droplet and the flow over the droplet diminishes to negligible levels.

To illustrate the influence of the plate separation on the drop shape, in figure 8(*a*) we plot contact line contours for plate separations $H/h = \infty, 10, 5$, for a droplet with representative capillary number $Ca = 0.14$. As the plate separation decreases from $H/h \to \infty$ to $H/h = 5$, the drop deformation decreases, resulting in a smaller extension in the y-direction as well as in the flow direction. For smaller plate separation, figure 8(*b*) shows the contact line contours for a droplet with capillary number $Ca = 0.07$ at $H/h = 2$ and 1.1. In this case, as the plate separation decreases the drop deformation increases resulting in a larger extension in both the y-direction and the flow direction.

With a basic understanding of the displacement process for viscous drops with $\lambda = 1$, we turn to droplets with higher viscosity ratio λ. For the sake of brevity, we restrict our attention to the influence of the plate separation H/h for high-viscosity droplets. Figure 9 shows the critical Ca versus contact angle hysteresis for a droplet with $\lambda = 10$ and $\theta_A = 90°$, for unconstrained optimization at several different plate

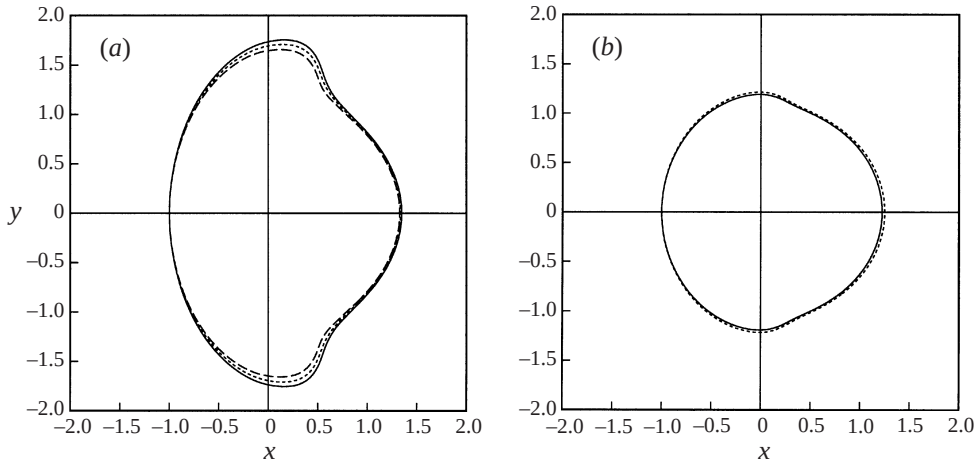

FIGURE 8. Equilibrium shapes for droplets in pressure-driven flows for $\lambda = 1$, $\theta_A = 90°$, for the unconstrained optimization problem and for different plate separations H/h. (*a*) The optimal shape of the contact line for $Ca = 0.14$. Plate separations H/h: ——, ∞; - - - -, 10; – – – –, 5. (*b*) As in (*a*) but for $Ca = 0.07$. Plate separations H/h: ——, 2; - - - -, 1.1.

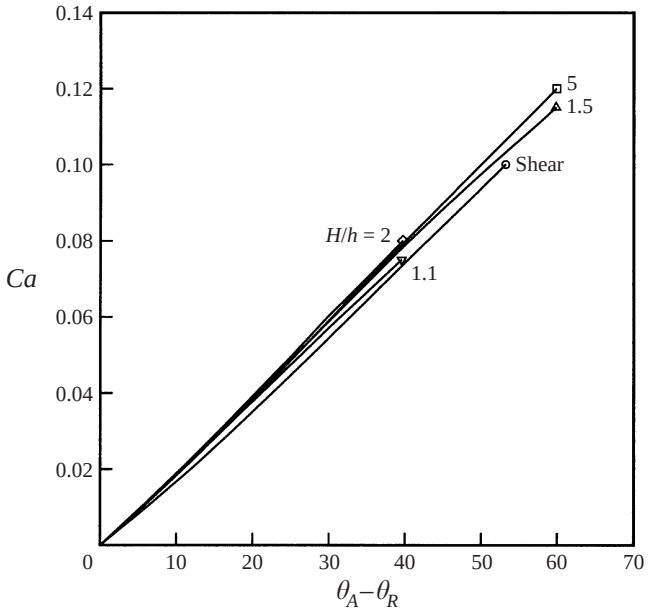

FIGURE 9. Critical capillary number Ca versus hysteresis $\theta_A - \theta_R$ for a droplet with $\lambda = 10$ and $\theta_A = 90°$, for the unconstrained optimization and for different plate separations H/h.

separations. This figure shows that the effect of plate spacing here is similar to that for $\lambda = 1$ droplets with a maximum in the critical flow rate near $H/h = 2$. The influence of the plate spacing on drop shape is illustrated in figure 10 which shows the contact line contours for plate separation $H/h = \infty, 5, 1.5$ at a capillary number $Ca = 0.10$. In this figure, the deformation of a high-viscosity droplet exhibits a stronger sensitivity to plate spacing than the $\lambda = 1$ droplet. The physical discussion and scaling analysis presented earlier help to explain the distinct contours arising

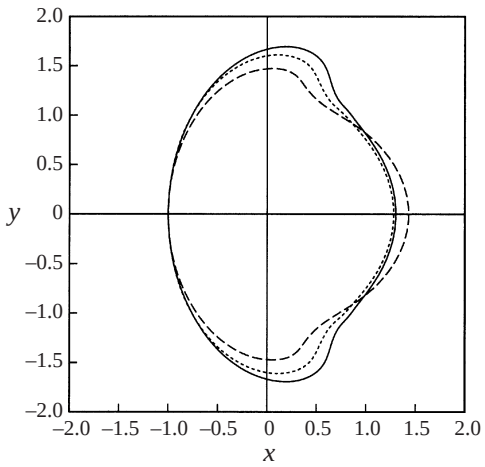

FIGURE 10. The optimal shape of the contact line for droplets in pressure-driven flows for $\lambda = 10$, $\theta_A = 90°$, $Ca = 0.10$, for the unconstrained optimization problem and for plate separations H/h: ——, ∞; - - - -, 5; – – – –, 1.5.

at different plate separation. For large plate separation, the increased width of the droplet increases the interfacial force while the dominant shear force is insensitive to width for a given contact area. In this case, the viscous drop can increase its stability by spreading in the lateral direction. By contrast, when the position of the upper plate approaches the drop height, lateral extension is less desirable, because the pressure force and interfacial force are both proportional to the width of the droplet. Therefore, when $H/h \to 1$, the viscous droplet experiences smaller lateral extension and greater flow elongation, as shown in figure 10. Additional results for high-viscosity droplets may be found in Dimitrakopoulos (1998).

3.2. *Displacement of inviscid droplets* ($\lambda = 0$)

Continuing our discussion of viscosity effects, we examine the case of inviscid droplets with $\lambda = 0$. Figure 11(a, b) shows the contact line contours and drop profiles for unconstrained optimization of inviscid droplets with contact angle $\theta_A = 90°$ at plate spacing $H/h = 2$. The distribution of contact angles around the drop contours is shown in figure 11(c), while three-dimensional views of the droplet for a typical Ca are shown in figure 11(d, e). The droplet behaviour illustrated in this figure is similar to that observed for the viscous droplets, with a few notable changes. Comparing the unconstrained contours for the cases $\lambda = 0$ and $\lambda = 1$, we see less deformation and lateral extension for the inviscid droplet. For inviscid droplets, the net hydrodynamic force is associated purely with pressure forces, and there is less to be gained from increased droplet width. The lateral and flow extension is a consequence of the reduction in the upstream contact angle and the need to preserve the total volume of the droplet. Of course, at a given Ca, there is less overall deformation, because the pressure force alone is smaller than the combined pressure and viscous forces encountered previously for viscous droplets. The inviscid y-constrained droplets (not shown) continue this trend with less overall extension in the flow direction than for the equivalent viscous droplets. In addition, as for the viscous droplets, the critical capillary number Ca for the y-constrained inviscid droplets is consistently smaller than for the unconstrained droplets. These results are given in Dimitrakopoulos (1998).

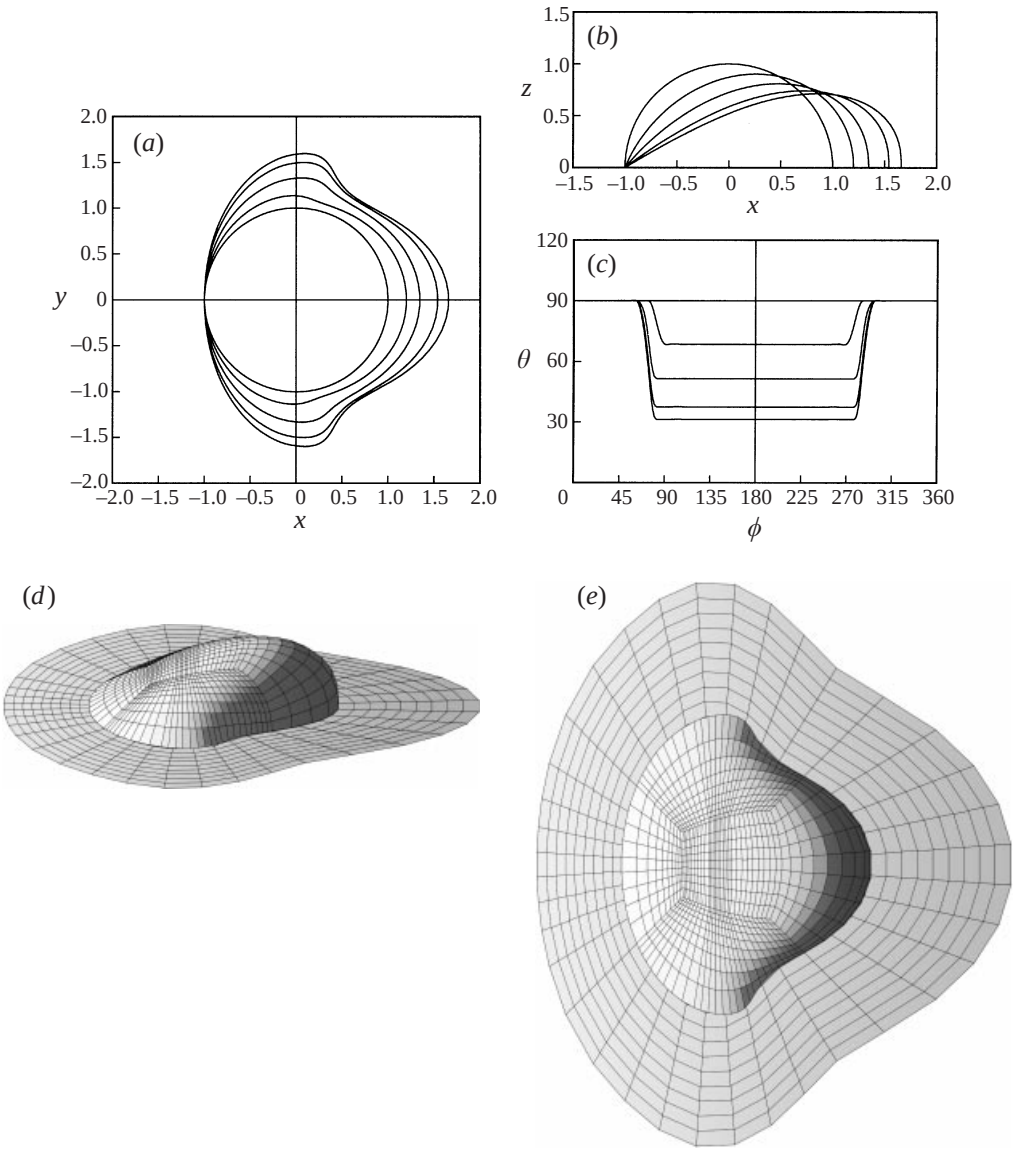

FIGURE 11. Equilibrium shapes for inviscid droplets ($\lambda = 0$) in pressure-driven flows with advancing contact angle $\theta_A = 90°$, for $H/h = 2$ and for the unconstrained optimization problem. For (a–c) the capillary number is $Ca = 0, 0.10, 0.20, 0.30, 0.35$. ($a$) The optimal shape of the contact line. (b) The cross-section of the drop surface with the plane $y = 0$. (c) The variation of the contact angle θ as a function of the azimuthal angle ϕ. (d, e) The drop surface for capillary number $Ca = 0.35$.

Next, we examine the effect of the advancing contact angle θ_A on the critical capillary number. We restrict our attention to the unconstrained problem, but consider two different plate separations, $H/h = 5$ and $H/h = 1.1$, because these two configurations show significantly different behaviour. Figure 12(a) shows the critical Ca for plate spacing $H/h = 5$ with curves for several different contact angles θ_A. Here, the effect of θ_A on the yield condition for inviscid droplets is dramatically different from that for viscous droplets. For inviscid droplets and a given hysteresis $\theta_A - \theta_R$, increasing θ_A decreases the critical shear rate. By contrast, for viscous droplets increasing θ_A from

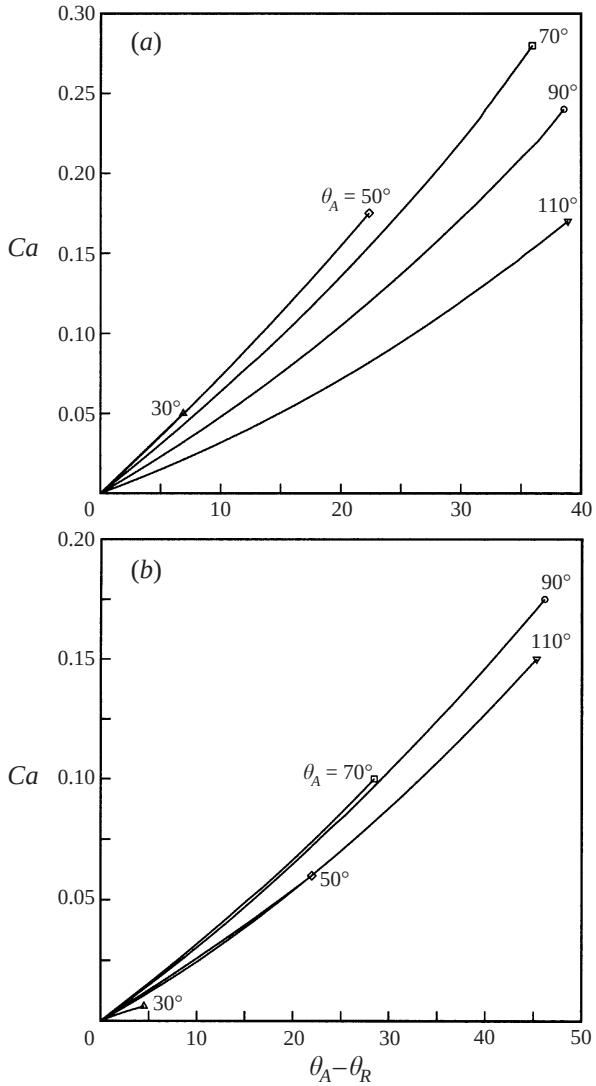

FIGURE 12. Critical capillary number Ca versus hysteresis $\theta_A - \theta_R$ for viscosity ratio $\lambda = 0$, for the unconstrained optimization problem and for different advancing angles θ_A. Plate separation: (*a*) $H/h = 5$, (*b*) $H/h = 1.1$.

small values increases the critical shear rate. This difference in behaviour is much more pronounced at small θ_A and large H/h. In our second plot, figure 12(*b*), we show the dependence of yield condition on θ_A for a small plate separation $H/h = 1.1$. In this figure, at small θ_A, the influence of the contact angle is reversed, with increases in θ_A producing an increase in critical Ca.

This change in behaviour can be easily explained if one considers the individual contributions to the hydrodynamic force. For an inviscid droplet, the viscous shear stress is identically zero, while the pressure force is composed of two distinct components. In our earlier discussion, we noted that the pressure force associated with the

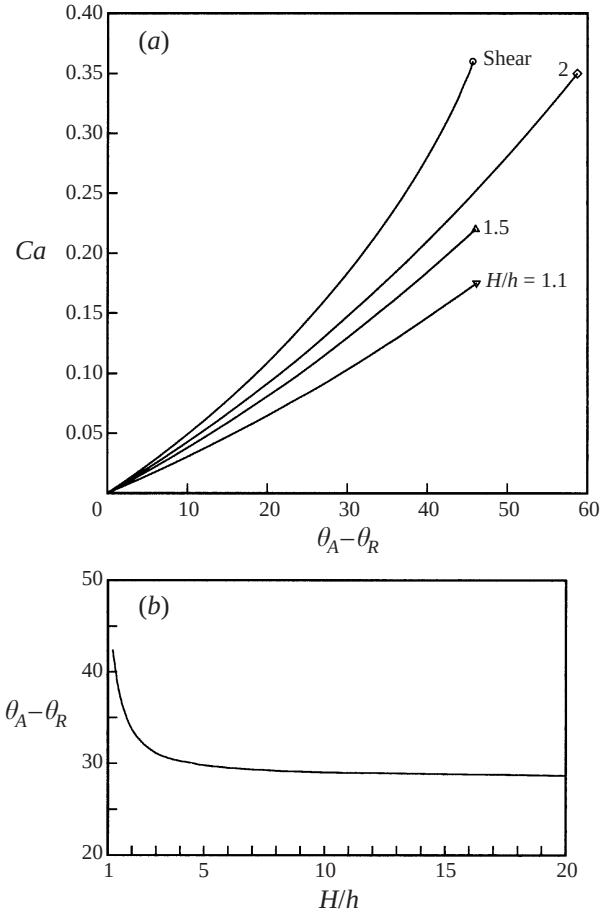

FIGURE 13. Influence of the plate separation H/h. (*a*) Critical capillary number Ca versus hysteresis $\theta_A - \theta_R$ for a droplet with $\lambda = 0$ and $\theta_A = 90°$, for the unconstrained optimization and for different plate separations H/h. (*b*) Contact angle hysteresis $\theta_A - \theta_R$ versus plate separation H/h for a droplet with $\lambda = 0$ and $\theta_A = 90°$, for $Ca = 0.17$ and for the unconstrained optimization.

undisturbed pressure gradient scales as $\tau_\infty a^2 \theta_A^{-2/3} (H/h)^{-1}$, while the pressure force arising from the disturbance of the base flow scales as $\tau_\infty a^2 \theta_A^{4/3}$. These pressure forces must be balanced by the interfacial force which scales as $(\theta_A - \theta_R)\gamma a \theta_A^{2/3}$.

For large plate spacing, the base pressure gradient is quite weak, and the dominant pressure force is associated with the disturbance of the base flow. Balancing this pressure force with the interfacial force yields the scaling for the critical Ca

$$Ca_{asym\_inviscid} \sim \theta_A^{-2/3} (\theta_A - \theta_R) \quad \text{for} \quad H/h \gg 1. \tag{10}$$

This shows that the critical flow rate decreases with increasing θ_A as illustrated in figure 12(*a*).

For small plate spacing, the dominant pressure force is associated with the base pressure gradient. Balancing this force with the interfacial force yields the scaling

$$Ca_{asym\_inviscid} \sim \theta_A^{4/3} (\theta_A - \theta_R) \quad \text{for} \quad H/h \sim 1. \tag{11}$$

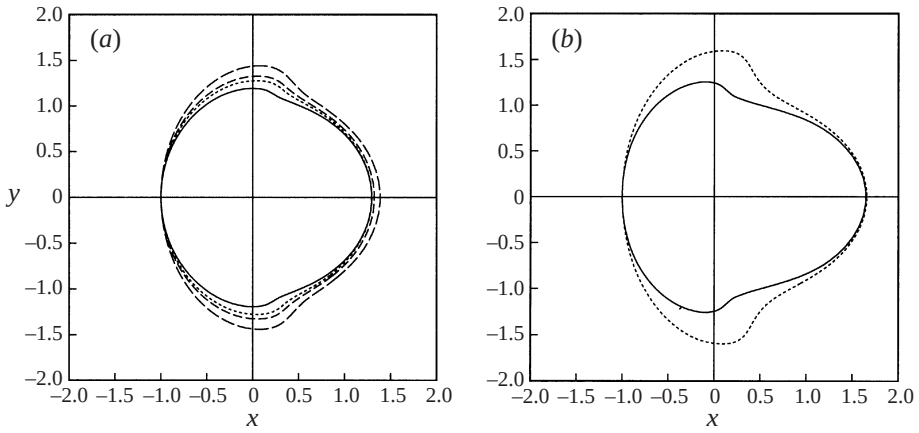

FIGURE 14. The optimal shape of the contact line for droplets in pressure-driven flows for $\lambda = 0$, $\theta_A = 90°$, for the unconstrained optimization problem and for different plate separations H/h. The capillary number is (*a*) $Ca = 0.17$, (*b*) $Ca = 0.35$. Plate separations H/h: ——, ∞; - - - -, 2; – – – –, 1.5; ——————, 1.1.

Now the critical flow rate increases with increasing θ_A as illustrated in figure 12(*b*). The behaviour in this figure is analogous to that observed earlier for viscous drops, because the scaling for the gradient term in the pressure force, for small plate spacing, is similar to that for the viscous shear stress. As in the viscous case, the decline in Ca for θ_A above 90° arises because the interfacial force reaches its maximum at $\theta_A = 90°$.

Next, we examine the influence of plate spacing in detail for a single value of $\theta_A = 90°$. For brevity, we present only the results for the unconstrained optimal contact lines. Figure 13(*a*) shows the critical Ca as a function of hysteresis for four different plate separations H/h, while figure 13(*b*) shows the critical hysteresis as a function of plate spacing for a single Ca. These curves show that the effect of plate separation H/h for inviscid drops is significantly different from that shown earlier for viscous drops. The net hydrodynamic force on the inviscid droplet is solely due to the pressure force, and it increases monotonically with reduced plate spacing. The critical curves for the yield conditions in figure 13 show a corresponding monotonic behaviour with easier displacement of the droplets as the plate separation is reduced.

To illustrate the effect of the plate separation H/h on the shape of an inviscid droplet, figure 14(*a*) shows the contact line contours for inviscid droplets for a specified Ca at several plate separations H/h. For all contours, the droplets must spread over the solid surface to accommodate the fixed fluid volume as the leading contact angle is reduced. At large plate separation (solid line for $H/h \to \infty$), the inviscid droplets spread primarily in the flow direction with increasing elongation for increasing Ca. In this regime, the base pressure gradient is negligible, and there is no penalty for extension in the flow direction. For small plate separation, the pressure gradient term is the dominant hydrodynamic force, and the droplets extend in the lateral direction to avoid this large pressure force. The pressure force does increase owing to the increased frontal area, but this is offset by the proportionate increase in interfacial force. This behaviour is more pronounced at higher flow rates as shown in figure 14(*b*). Additional discussion on plate spacing and inviscid droplets

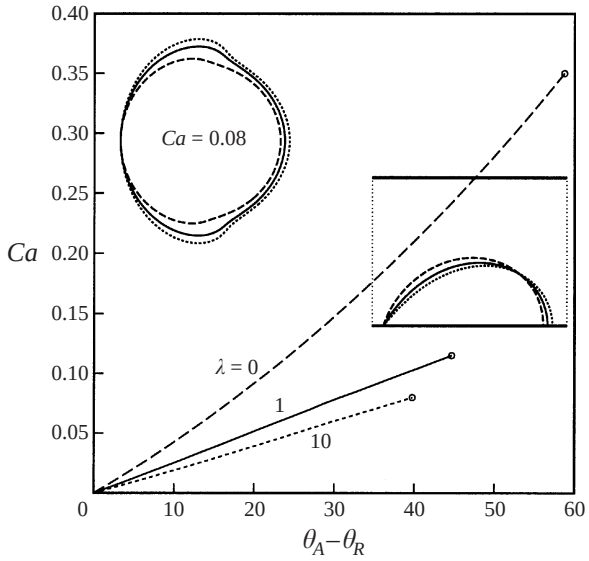

FIGURE 15. Critical capillary number Ca versus hysteresis $\theta_A - \theta_R$ for $\theta_A = 90°$, $H/h = 2$ and for several viscosity ratios, for the unconstrained optimal contact lines. Also shown are the shapes of the contact line as well as the drop profiles for $Ca = 0.08$. Viscosity ratios λ: ——, 1; - - - -, 10; – – – –, 0.

including the case of y-constrained optimization may be found in Dimitrakopoulos (1998).

3.3. *Influence of the viscosity ratio* λ

In this section, we collect results from calculations for $\lambda = 0, 1, 10$ to highlight the influence of viscosity ratio on drop displacement at a fixed plate spacing. In figure 15 we plot the critical Ca as a function of hysteresis $\theta_A - \theta_R$ at plate separation $H/h = 2$ for the unconstrained optimization. The insets show the optimal contact lines and drop profiles for the different droplets. For the large-contact-angle ($\theta_A = 90°$) droplets considered here, the inviscid droplets as well as the high-viscosity droplets show a significant departure from the $\lambda = 1$ results. Clearly the effects of the droplet viscosity should not be discounted for fluids with $\lambda > 1$ or $\lambda < 1$, and projections based on $\lambda = 1$ may give only qualitative predictions for inviscid or high-viscosity fluids. The contact line contours shown in figure 15 nicely illustrate the fact that, as the droplet viscosity increases, the unconstrained contact lines exhibit greater lateral extension.

To offer further insight into the combined effects of viscosity ratio and plate separation, in figure 16 we plot the critical Ca for different λ at two extremes $H/h \to \infty$ and $H/h = 1.1$. We show only the results for unconstrained optimization here. From these curves, we observe that the effect of viscosity ratio for $H/h = 2$ is quite close to the result for infinite plate separation or simple shear flow. By contrast, for very small plate separation $H/h = 1.1$, we see a noticeable difference with the curves for $\lambda = 0$ more closely approaching those of the viscous droplets. This result is to be anticipated based on the foregoing discussion of scaling behaviour in the limit $H/h \to 1$.

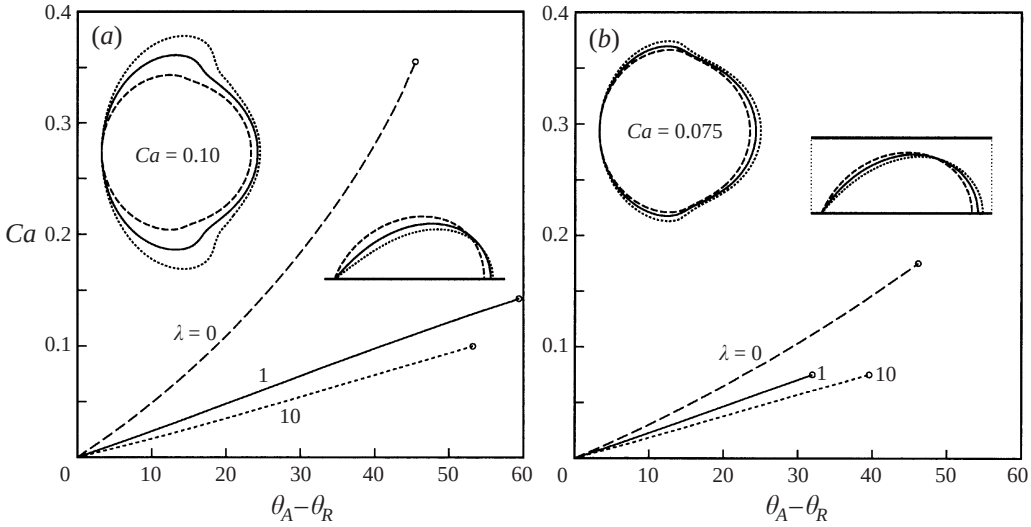

FIGURE 16. Critical capillary number Ca versus hysteresis $\theta_A - \theta_R$ for $\theta_A = 90°$, for the unconstrained optimal contact line and for several viscosity ratios. (*a*) The plate spacing is $H/h \to \infty$. Also shown are the shapes of the contact line as well as the drop profiles for $Ca = 0.10$. (*b*) As in (*a*) but for $H/h = 1.1$ and $Ca = 0.075$. Viscosity ratios λ: ——, 1; - - - -, 10; – – – –, 0.

3.4. *Comparison with experimental observations*

We conclude our study of drop displacement in pressure-driven flows by offering a qualitative comparison of our results with experimental observations. First, we note that there appear to be no detailed experimental results available for droplet shapes or yield conditions for drop displacement in pressure-driven flows. The majority of experiments have focused on the displacement of droplets on inclined surfaces due to the action of gravity. Given these circumstances, we attempted some informal visualization studies for viscous displacement in a parallel plate geometry. These experiments were of limited extent and addressed only the qualitative issues concerning droplet shape. Figure 17(*a*) shows the deformed interface shape for an stationary air bubble attached to a Plexiglas substrate immersed in a flowing glycerol solution. The experimental procedure here matched that described for the y-constrained optimization in DH2, § 3.1. To compare this experimental observation with our computational results, in figure 17(*b*) we present the surface of an inviscid droplet ($\lambda = 0$) with advancing angle $\theta_A = 90°$, for plate separation $H/h = 2$, for the stated optimization problem and a representative capillary number. Our computational results match the experiment in a number of key features including elongation in the flow direction, asymmetry in the flow direction and in the indentation and inflection points on the sides of the bubble.

The prediction of the yield stress for droplet displacement is probably the most important issue addressed in this paper. Unfortunately, there are no experimental results with which we may make direct comparison. The only available computational predictions are our own results for drop displacement in viscous shear flows (DH2). As noted above, we have shown that our present results for pressure-driven flows smoothly approach the shear flow results as $H/h \to \infty$. We note that those earlier results showed excellent agreement with the theoretical predictions of Dussan V. (1987) in the appropriate asymptotic limits.

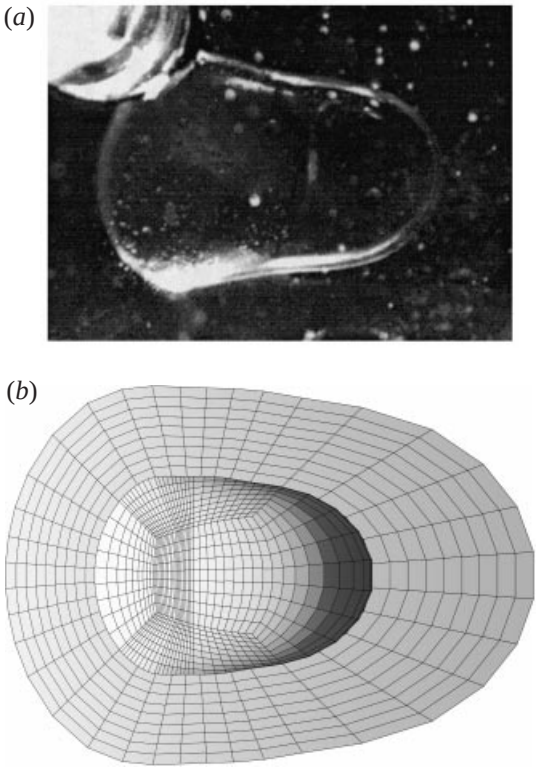

FIGURE 17. Comparison with experimental results. (*a*) A stationary air bubble attached to a Plexiglas substrate immersed in a flowing glycerol solution. (*b*) The surface of an inviscid droplet ($\lambda = 0$) with advancing contact angle $\theta_A = 90^\circ$, for plate spacing $H/h = 2$, capillary number $Ca = 0.25$ and for the y-constrained optimization problem.

4. Conclusions

In this paper we have conducted an extensive study of the drop displacement problem for three-dimensional droplets in pressure-driven flows. We summarize briefly some of the more important conclusions.

(i) The contact line contours for real droplets show fore-and-aft asymmetry with a distorted shape not well represented by simple circular/elliptical planforms. The distorted profiles allow sharp jumps in contact angle which increases the ability of a droplet to adhere to a surface. The y-constrained contact line contours predicted by the simulations show good qualitative agreement with experimental observations.

(ii) The yield stress predicted by the unconstrained optimization provides an upper bound on the yield condition for a droplet on a solid substrate. Alternative droplet configurations resulting from the y-constrained optimization show only a small change in the predicted yield stress compared to the unconstrained case. Computations based on circular contact lines show a significant reduction in the predicted yield stress.

(iii) Viscosity ratio plays an important role for viscous droplets. As the viscosity of a droplet increases, the critical flow rate decreases (i.e. the displacement becomes easier). This is consistent with our previous results for shear flows, which represent the limit of infinite plate spacing. As the plate spacing is reduced, the critical flow rate increases until a maximum value is reached, whereupon further reduction decreases

the critical flow rate. The effects of both viscosity ratio and plate separation are more pronounced for high contact angles.

(iv) Inviscid droplets (or bubbles) show behaviour dramatically different from that of viscous droplets. A significantly high flow rate is required for drop displacement, but this critical flow rate decreases monotonically as the distance between the plates decreases. The displacement of inviscid droplets is strongly affected by the change in the character of the pressure force as the plate spacing is reduced.

This work was supported by the National Science Foundation. Panagiotis Dimitrakopoulos acknowledges the support of H. G. Drickamer fellowship from the Department of Chemical Engineering at the University of Illinois. The computations were performed on the multiprocessor computers SGI Cray Origin 2000 and HP-Convex Exemplar SPP 2000 provided by the National Center for Supercomputing Applications.

Appendix. Constraints on the exterior Reynolds number for $\lambda \ll 1$

In this Appendix, we consider the conditions required for validity of the Stokes flow equations. For any value of the viscosity ratio λ, the conditions for low Reynolds number in both the interior and exterior flows are

$$Re_2 \equiv \frac{\rho_2 u_2 a}{\mu_2} = \frac{\rho_2 G a^2}{\mu} \ll 1 \tag{A 1}$$

and

$$Re_1 \equiv \frac{\rho_1 u_1 a}{\mu_1} = \frac{\rho_1 G a^2}{\lambda \mu} = Re_2 \frac{\rho_1}{\rho_2} \frac{1}{\lambda} \ll 1. \tag{A 2}$$

For density ratio ρ_1/ρ_2 and viscosity ratio λ of $O(1)$ or higher, these conditions are both satisfied if $Re_2 \ll 1$. Therefore, in this case, when the inducing outer flow is Stokes, the resultant inner flow is Stokes as well.

For low viscosity ratio ($\lambda \ll 1$), the condition (A 2) requires

$$Re_2 \frac{\rho_1}{\rho_2} \ll \lambda \ll 1, \tag{A 3}$$

which seems to impose a severe constraint on the exterior Reynolds number. The main point of this Appendix is to show that it is sufficient for the two conditions $Re_2 \ll 1$ and $\lambda \ll 1$ to be satisfied independently, without any condition on the relative magnitude.

For the case of gas bubbles in a liquid, because of the small density ratio ρ_1/ρ_2, the condition (A 3) is easily satisfied without undue restriction on Re_2. While the present study has not formally included the effects of gravitational forces, the density difference has no effect on the dynamics as long as the Bond number $B_d = (\rho_1 - \rho_2) g a^2/\gamma$ is small, as is usually the case for small droplets.

When the density ratio is of $O(1)$, there are a number of interesting applications where $\lambda \ll 1$, and the condition (A 3) is not satisfied. In these circumstances, we find that our results for the $\lambda = 0$ droplets remain valid, independent of the interior Reynolds number. The computations for $\lambda = 0$ require that the exterior Reynolds number remains small, and also require the boundary conditions $\tau_1 = 0$ and $\Delta p_1 = 0$ at the fluid–fluid interface. More specifically, we require that the inner shear stress τ_1 and pressure change Δp_1 are small compared to exterior stresses which scale as $\tau_\infty = \mu G$.

For arbitrary interior Reynolds number, there are two contributions to these stresses: inertial terms and viscous terms. Consider the case of finite contact angle θ_A. The inertial terms scale as $\rho u_1^2 \sim \rho u_2^2$, where $u_2 \sim Ga$. This contribution is always small when the exterior Reynolds number is small, i.e.

$$\frac{\Delta p_1}{\tau_\infty} \sim \frac{\rho u_2^2}{\mu G} \sim Re_2 \ll 1. \tag{A 4}$$

The viscous terms scale as $\lambda\mu u_1/\ell \sim \lambda\mu u_2/\ell$ for some length scale ℓ. When the interior Reynolds number is small, the length scale is a and the ratio of interior viscous forces to exterior viscous forces is just $\tau_1/\tau_\infty \sim \lambda \ll 1$. When the interior Reynolds number is large, interior interfacial boundary layers may develop, and the length scale ℓ is dictated by the balance between viscous and inertial forces. If the boundary layer thickness scales as $\ell \sim (\lambda\mu a/\rho u_1)^{1/2}$, then the interior shear stress and pressure changes scale as

$$\frac{\tau_1}{\tau_\infty} \sim \lambda^{1/2} Re_2^{1/2} \ll 1. \tag{A 5}$$

The local boundary layer thickness will vary somewhat dependent upon the functional form of $u_2(x)$; however, the basic scaling (A 5) remains the same. Furthermore, the viscous terms cannot exceed the magnitude of the inertial forces and thus they are bounded by the smaller of (A 4) or (A 5). The analysis above may be repeated for asymptotically small contact angle θ_A, with both the velocity u_1 and the length scale ℓ reduced by a factor θ_A. The final conclusion is the same.

In summary, the boundary conditions at the interface ($\tau_1 = 0$ and $\Delta p_1 = 0$) remain valid for arbitrary interior Reynolds number Re_1, as long as the individual constraints $Re_2 \ll 1$ and $\lambda \ll 1$ are satisfied.

REFERENCES

Dimitrakopoulos, P. 1998 Displacement of fluid droplets from solid surfaces. PhD thesis, University of Illinois.

Dimitrakopoulos, P. & Higdon, J. J. L. 1997 Displacement of fluid droplets from solid surfaces in low-Reynolds-number shear flows. *J. Fluid Mech* **336**, 351–378 (referred to herein as DH1).

Dimitrakopoulos, P. & Higdon, J. J. L. 1998 On the displacement of three-dimensional fluid droplets from solid surfaces in low-Reynolds-number shear flows. *J. Fluid Mech.* **377**, 189–222 (referred to herein as DH2).

Dimitrakopoulos, P. & Higdon, J. J. L. 1999 On the gravitational displacement of three-dimensional fluid droplets from inclined solid surfaces. *J. Fluid Mech.* **395**, 181–209.

Dussan V., E. B. 1987 On the ability of drops to stick to surfaces of solids. Part 3. The influences of the motion of the surrounding fluid on dislodging drops. *J. Fluid Mech.* **174**, 381–397.

Li, X. & Pozrikidis, C. 1996 Shear flow over a liquid drop adhering to a solid surface. *J. Fluid Mech.* **307**, 167–190.

Schleizer, A. D. & Bonnecaze, R. T. 1999 Displacement of a two-dimensional immiscible droplet adhering to a wall in shear and pressure-driven flows. *J. Fluid Mech.* **383**, 29–54.

Yon, S. & Pozrikidis, C. 1999 Deformation of a liquid drop adhering to a plane wall: Significance of the drop viscosity and the effect of an insoluble surfactant. *Phys. Fluids* **11**, 1297–1308.